

Reconstructing the Anisotropic Ultra-long Wavelength Spectra using a Single Antenna on Lunar-orbit

QIGE AO ^{1,2,3} FUREN DENG ^{1,3} YIDONG XU ^{1,4} BIN YUE ^{1,4} HUANYUAN SHAN ^{2,3,4} AND XUELEI CHEN ^{1,3,4}

¹National Astronomical Observatories, Chinese Academy of Sciences, 20A Datun Road, Chaoyang District, Beijing 100101, China

²Shanghai Astronomical Observatory, Chinese Academy of Sciences, 80 Nandan Road, Xuhui District, 200030, China

³School of Astronomy and Space Science, University of Chinese Academy of Sciences, No.1 Yanqihu East Rd, Huairou District, Beijing 101408, China

⁴Key Laboratory of Radio Astronomy and Technology, Chinese Academy of Sciences, 20A Datun Road, Chaoyang District, Beijing 100101, China

ABSTRACT

The ultra-long wavelength sky ($\nu \lesssim 30$ MHz) is still largely unexplored, as the electromagnetic wave is heavily absorbed and distorted by the ionosphere on Earth. The far-side of the Moon, either in lunar-orbit or on lunar-surface, is the ideal site for observations in this band, and the upcoming Moon-based interferometers will obtain multi-frequency high-resolution sky maps. Making use of the lunar occultation of the sky and the anisotropy of antenna primary beam response, we propose a novel method to reconstruct the ultra-long wavelength spectral shape in multiple directions in the sky using only one antenna on lunar orbit. We apply the method to one antenna on one of the nine daughter satellites of the proposed Discovering the Sky at Longest wavelength (DSL) project. Using simulated observation data between 1 - 30 MHz from one dipole antenna, we find that the spectra for different regions on the sky can be reconstructed very well and the free-free absorption feature in each region can be derived from the reconstructed spectra. This work demonstrates the feasibility to reconstruct the anisotropic ultra-long wavelength spectra with very limited instrumentation on a lunar-orbit, with mature technologies already in place. It extends the application of such kind of satellite in revealing the distribution of free electrons in the Galactic interstellar medium from the distribution of absorption features in the ultra-long wavelength sky.

Keywords: Radio astronomy (1338) — Radio continuum emission (1340) — Interstellar medium (847)
— Interstellar absorption (831)

1. INTRODUCTION

The ultra-long wavelength band (wavelength $\lambda \gtrsim 10$ m or frequency $\nu \lesssim 30$ MHz) is the remaining electromagnetic window that is still largely unexplored, particularly below $\lesssim 10$ MHz (e.g., Brown 1973; Cane 1979; Yates & Wielebinski 1967; Novaco & Brown 1978; Peterson & Webber 2002). Some proposed projects, for example FARSIDE (Burns et al. 2021a), DAPPER (Burns et al. 2021b), LuSEE-Lite/LuSEE-Night (Bale et al. 2023), et al., aim to carry out observations in the ultra-long wavelength band and reveal the new celestial objects and physical mechanisms in this band. Among these, the Discovering the Sky at Longest wavelength (DSL) is a

proposed upcoming lunar-orbit satellite array project. It is composed of one mother satellite, eight low-frequency daughter satellites that form a linear interferometer array to take images of the Universe between 0.1 MHz and 30 MHz, and another high-frequency satellite dedicated to precisely measure the global spectrum from 30 - 120 MHz (Chen et al. 2019; Chen et al. 2021). For the eight low-frequency satellites, each of them carries three pairs of orthogonal monopole antennas on the two sides of the satellite. Each pair of antennas acts as a short dipole that connects to an independent channel of the receiver, so they can work either as an interferometer or independently.

In early observations, it has been found that the global spectrum of radio background has a downturn at ~ 3 – 5 MHz. This is ascribed to the free-free absorption by free electrons in the interstellar medium (ISM) of our

Milky Way (e.g., Ellis & Hamilton 1966; Alexander & Stone 1965; Smith 1965; Alexander et al. 1969; Brown 1973; Novaco & Brown 1978). This is also found in the frequency spectrum of the radio sky anisotropy (Page et al. 2022) and can put constraints on sky models that involve free-free absorption (Bassett et al. 2023). Cong et al. (2021) developed a radio sky model, the Ultra-Long wavelength Sky model with Absorption (ULSA), which involves this absorption based on Milky Way electron model (Cordes & Lazio 2002, 2003), so it is valid down to $\lesssim 10$ MHz. ULSA predicts that, in the ultra-long wavelength band, the sky morphology is rather different from higher frequencies. The Galactic plane is darker than high Galactic latitude regions, and the electron structures may leave shadows and bright spots on the sky. This absorption mechanism provides an opportunity to reconstruct the 3-D free-electron distribution from ultra-long wavelength observations (Cong et al. 2022).

Although the DSL low-frequency daughter satellites are designed to make images of the sky from cross-correlation measurements between them, each of them also individually records the global spectrum (auto-correlation) from 0.1 - 30 MHz with high frequency resolution. The observed global spectrum varies with the pointing direction of the antenna, not only because the primary beam response is not perfectly isotropic, but also and more importantly, the Moon blocks the radiation in the opposite direction of the antenna pointing. As the satellite orbits the Moon, the varying spectra received by the antenna encodes information on the spatial variation of the spectra in the sky. It means that, even in the single antenna mode, a lunar-orbit satellite has the ability to resolve the anisotropy in the spectrum. Especially in the ultra-long wavelength band, one could potentially reveal the anisotropic absorption feature using one single antenna on the lunar orbit.

In this paper, we investigate the feasibility of reconstructing parameterized spectra for different directions in the sky, from mock observation data from a single antenna on one of the DSL low-frequency satellites. If applied to real data, the free-free absorption to ultra-long wavelength radiation from different sky directions can be derived from the reconstructed anisotropic spectra, and the spatial distribution of the ISM free electrons can be learned from the single antenna observations in a lunar orbit. The layout of this paper is as follows. We first introduce our method to reconstruct the spectra of different sky regions in Section 2, and then in Section 3 we present our results of the estimated parameter values and uncertainties. In Section 4, we summarize and discuss our results.

2. METHODS

In this section, we first generate mock time-ordered sky temperature data (TOD) from the ULSA sky model, considering the orbital motion and the natural precession of the satellites, the varying Moon blockage and antenna pointing, and the beam response. We choose equally-separated $N_\nu = 59$ frequency points between 1 MHz and 30 MHz, each has a width of 0.5 MHz. By design, the DSL low-frequency satellites can measure the electromagnetic radiation down to 0.1 MHz, however, the spectral shape may become complicated below ~ 1 MHz, because at such low frequencies, the radiation would be dominated by the Sun and sources quite close to the Solar system due to the strong absorption (Jester & Falcke 2009; Cong et al. 2021). To avoid complicating the problem, here we limit our investigation in the frequency of 1 - 30 MHz. We re-bin the TOD to generate the mock data sample. Then we parameterize the spectrum, using a turnover frequency to describe the absorption. Finally, we divide the sky into multiple regions and reconstruct the parameterized spectrum for each region from the mock data sample.

2.1. The mock observational data sample

In our simulation setup, the Moon is a sphere with a radius of 1737.47 km. The satellite moves around the Moon in a circular orbit at a constant height of 300 km from the Moon surface. The period of this motion is about 2.3 hr. According to the DSL design, the orbital plane of the satellite has an inclination angle of 30° with respect to the lunar equator plane, and the orbital plane precesses relative to the lunar equator plane with a period of 1.3 yr (Chen et al. 2021). In this study, we use only one of the antennas, and assume that the antenna always points to anti-selenocenter. When it moves along the orbit, the antenna pointing changes with time, and the Moon blocks the sky area in the opposite direction of the pointing.

Suppose at time t the antenna is pointing to the direction $\hat{\mathbf{k}}_t$ on sky, then the antenna temperature at frequency ν is (Shi et al. 2022a),

$$T_{\text{TOD}}(\nu, t) = \frac{\int S(\hat{\mathbf{k}}, \hat{\mathbf{k}}_t) B(\hat{\mathbf{k}}, \hat{\mathbf{k}}_t) T_{\text{sky}}(\nu, \hat{\mathbf{k}}) d\Omega(\hat{\mathbf{k}})}{\int B(\hat{\mathbf{k}}, \hat{\mathbf{k}}_t) d\Omega(\hat{\mathbf{k}})}. \quad (1)$$

$S(\hat{\mathbf{k}}, \hat{\mathbf{k}}_t)$ is the shade function. It describes the lunar occultation of sky. If radiation from direction $\hat{\mathbf{k}}$ is blocked by Moon, $S(\hat{\mathbf{k}}, \hat{\mathbf{k}}_t) = 0$; otherwise $S(\hat{\mathbf{k}}, \hat{\mathbf{k}}_t) = 1$. $B(\hat{\mathbf{k}}, \hat{\mathbf{k}}_t)$ is the antenna primary beam response. For a short dipole antenna, it is well-approximated as

$$B(\beta) = \sin^2(\beta), \quad (2)$$

where β is the included angle between the observing direction $\hat{\mathbf{k}}$ and the pointing direction of the antenna wire $\hat{\mathbf{k}}_t$. For such a beam response, the normalization factor in the denominator of Eq. (1) equals $8\pi/3$.

We use $T_{\text{sky}}(\nu, \hat{\mathbf{k}})$ from the ULSA sky model to generate the mock TOD. The input sky map adopts $N_{\text{side}} = 64$ in the HEALPix scheme (Gorski et al. 2005), corresponding to a resolution of about 55 arcmin, which is high enough for the following low-resolution reconstruction. In Fig. 1 we plot the input sky map at 5 MHz. The map shows clear free-free absorption features: the central Galactic plane is darker than around regions; there are some dark spots near the Galactic plane which are dense H II regions.

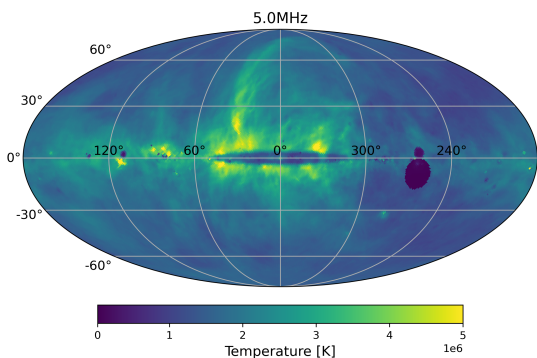


Figure 1. The sky map with frequency of 5 MHz in the Galactic coordinate system.

One precess period of DSL lasts 1.3 yr. If we sample an antenna temperature every 1 second, there will be 40,996,800 data points for each frequency; even if we just sample an antenna temperature point every 300 seconds, then for each frequency still there will be 136,656 data points. It is a huge load for later reconstruction procedure.

However, from Eq. (1), the antenna temperature varies only when the antenna pointing direction $\hat{\mathbf{k}}_t$ varies. To reduce the computational cost, we first pixelize the sky with the HEALPix scheme (Gorski et al. 2005) and adopt $N_{\text{side}} = 16$ (corresponding to a resolution 219.9 arcmin), then average the data points whose antenna pointings are in the same pixel.

In Fig. 2 we plot the number of data points in each pixel. It illustrates that the antenna fails to point at area with lunar declination $> 30^\circ$ or $< -30^\circ$. However, we note that each pixel just represents the central pointing direction of the antenna wire. The dipole antenna has a very wide beam coverage, and radiation from regions $> 30^\circ$ far from the lunar equator is still received by the antenna.

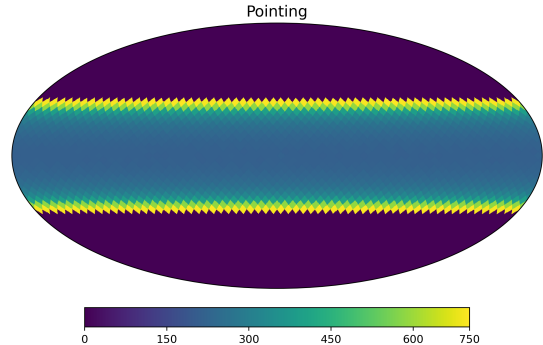


Figure 2. In one precession period, the antenna wire repeatedly points into same pixels on sky. This figure shows the number of pointing times for each sky pixel in *lunar equatorial coordinate system*. The sky is pixelized by HEALPix scheme with $N_{\text{side}} = 16$.

After the above procedure, the TOD is reduced to mock observation data sample with $N_{\text{data}} = 1600$ data points for each frequency. We plot the mock data sample on sky according to the antenna pointing in Fig. 3. Please note that this figure shows the averaged antenna temperature when the antenna points to the pixel. It is the full-sky temperature weighted by the primary beam response and Moon blockage, not the sky temperature from that pixel.

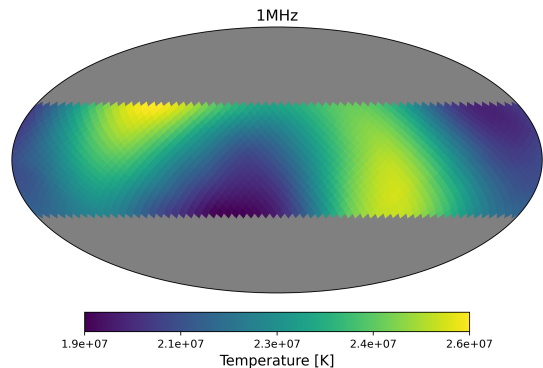


Figure 3. Our mock data simple for 1600 pixels on the sky in the lunar equatorial coordinate system. Note that this is not the sky temperature distribution. It is the mean antenna temperature when antenna wire is pointing into the corresponding pixel.

2.2. Reconstruction of parameterized spectrum from mock data sample

To reconstruct the spectra of different sky regions, we divide the sky into $N_{\text{region}} = 12$ regions (corresponding to $N_{\text{side}} = 1$ in HEALPix scheme), their positions on the sky is shown in Fig. 4. In principle, we can arbitrarily divide the sky into any number of regions

and each of them could have a different area. However, since a single dipole antenna has a very wide primary beam which, coupled with the large-scale Moon blockage, is inadequate for resolving small-scale sky temperature anisotropies, if the number of regions is too large, then the reconstructed spectra for neighboring regions would be highly degenerate. Therefore, in this work we only focus on large-scale anisotropies of the ultra-long wavelength spectrum, and adopt a modest choice of $N_{\text{region}} = 12$.

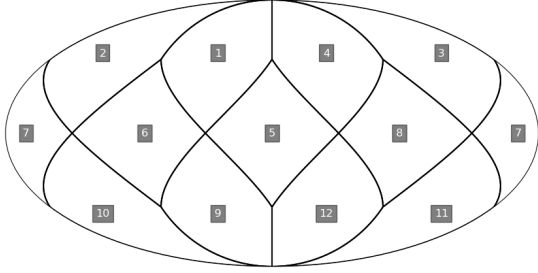


Figure 4. The position of 12 regions. The sequence of each region is marked in the picture.

Each of the mock observation data is approximated as the sum of contribution from all the 12 sky regions. For the i -th data point in the mock data simple,

$$T_i(\nu) \approx \frac{1}{(8\pi/3)} \sum_{j=1}^{N_{\text{region}}} \tilde{B}_j(\hat{\mathbf{k}}_i) \tilde{T}_j(\nu) \Delta\Omega_j, \quad (3)$$

where $\hat{\mathbf{k}}_i$ is the direction of the i -th point in the mock data sample; $\Delta\Omega_j = 4\pi/N_{\text{region}}$ is single pixel area.

$$\tilde{B}_j(\hat{\mathbf{k}}_i) = \frac{1}{\Delta\Omega_j} \int_{\Delta\Omega_j} S(\hat{\mathbf{k}}, \hat{\mathbf{k}}_i) B(\hat{\mathbf{k}}, \hat{\mathbf{k}}_i) d\Omega(\hat{\mathbf{k}}) \quad (4)$$

is kind of mean beam response within the j -th region.

We follow the spectral index form of equation (28) in Cong et al. (2021). For the j -th region, the frequency spectrum is

$$\tilde{T}_j(\nu) = A_j \left(\frac{\nu}{\nu_j} \right)^{a_j + b_j e^{-\frac{\nu}{\nu_j}}}, \quad (5)$$

where ν_j , a_j , b_j and A_j are the four parameters of our model. The parameter ν_j corresponds to a critical frequency. For $\nu \gg \nu_j$, spectrum index $\approx a_j$ and for $\nu \ll \nu_j$, spectrum index $\approx a_j + b_j$. So if the spectrum exhibits turnover feature, ν_j is just the turnover frequency. In order to have a better result we fit the log-form of this equation in this work. The form is transformed into

$$\log \tilde{T}_j(\nu) = \log A_j + \left(a_j + b_j e^{-\frac{\nu}{\nu_j}} \right) \log \left(\frac{\nu}{\nu_j} \right). \quad (6)$$

However, due to the complicated distribution of emissivity and electron distribution, the spectrum of ULSA model can not be fitted perfectly by above formula. But we check that, for the 12 regions, at $\nu \gtrsim 1$ MHz, their frequency spectrum can be fitted by Eq. (6) with errors $\lesssim 10\%$.

We then perform the reconstruction of the frequency spectrum for 12 regions from the mock data sample, using the Markov Chain Monte Carlo (MCMC) method with EMCEE (Foreman-Mackey et al. 2013). The spectrum of each region is described by four parameters, so there are 48 parameters in total.

The likelihood function is

$$L(\boldsymbol{\theta}|\mathbf{x}) = \prod_{j=1}^{N_{\text{data}}} \frac{1}{(2\pi)^{\frac{N_{\text{data}}}{2}} |\boldsymbol{\Sigma}|^{\frac{1}{2}}} \exp\left(-\frac{1}{2}(\mathbf{x} - \boldsymbol{\mu}(\boldsymbol{\theta}))^T \boldsymbol{\Sigma}^{-1} (\mathbf{x} - \boldsymbol{\mu}(\boldsymbol{\theta}))\right), \quad (7)$$

where \mathbf{x} is the mock data set, and $\boldsymbol{\mu}(\boldsymbol{\theta})$ is the modeled antenna temperature given by Eq. (3), corresponding to parameter set $\boldsymbol{\theta}$; $\boldsymbol{\Sigma}$ is the covariance matrix containing errors that will be introduced in next subsection.

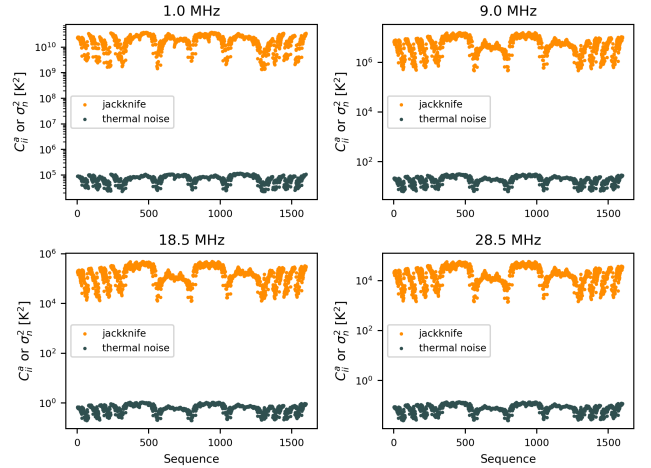


Figure 5. The errors described by Eq. (12) compared with thermal noise.

2.3. The errors

The mock data sample has thermal noise that follows Gaussian distribution with standard deviation being (for simplicity we ignore the subscript ν for all formulae in this subsection)

$$\sigma_n = \frac{T_{\text{sys}}}{\sqrt{\Delta\nu t_{\text{int}}}}, \quad (8)$$

where t_{int} is the integration time of each data point, and $\Delta\nu = 0.5$ MHz is width of each frequency point. The covariance matrix that describes thermal noise

$$C_{ij}^n = \begin{cases} \sigma_n^2, & i = j \\ 0, & i \neq j. \end{cases} \quad (9)$$

The system temperature T_{sys} has contributions from both the sky radiation and the receiver noise,

$$T_{\text{sys}} = T_{\text{rcv}} + \bar{T}_{\text{sky},i}. \quad (10)$$

$\bar{T}_{\text{sky},i}$ is the mean brightness temperature of the sky as average over the beam of the antenna pointing to the direction of the i -th mock data. T_{rcv} is the effective temperature of receiver noise. It can be approximated as (Shi et al. 2022b)

$$T_{\text{rcv}} = 6.61 \times 10^3 \left(\frac{\lambda}{10 \text{ m}} \right)^2 \left(\frac{2.5 \text{ m}}{l_{\text{eff}}} \right)^2 [\text{K}], \quad (11)$$

where l_{eff} is the effective length of the antenna wire, it is assumed as 2.5 m here. Since each of our mock data samples is averaged from many TOD data points, its σ_n is further reduced by the square root of its TOD points number. We add the Gaussian realizations of the thermal noise to the mock data sample.

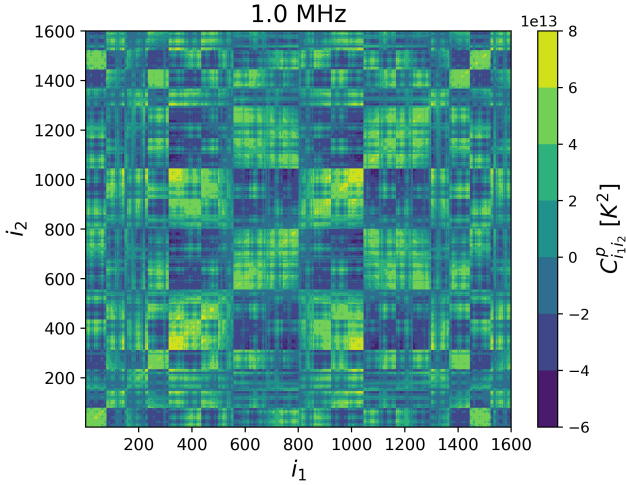


Figure 6. The covariance $C_{i_1 i_2}^p$ expressed by Eq. (21), for 1 MHz.

In addition to the thermal noise, there are other errors in our mock sample and in the model Eq. (3). When making the mock data sample, each of the data is obtained by averaging a limited number of TOD points in its pixel with a resolution of 219.9 arcmin. Such a data-averaging scheme results in a mock sample temperature that deviates from the antenna temperature calculated with assumption that the antenna points to the pixel center. This error vanishes if we have an infinite number of TOD points uniformly distributed in each pixel, and can be approximated as a Jackknife error. The covariance matrix is written as

$$C_{ij}^a = \begin{cases} \frac{N_i-1}{N_i} \sum_{k=1}^{N_i} (T_{ik} - T_i)^2, & i = j \\ 0, & i \neq j, \end{cases} \quad (12)$$

where the diagonal elements are estimated by the Jackknife method (Tukey 1958; Quenouille 1949).

$$T_i = \frac{1}{N_i} \sum_{k=1}^{N_i} T_{\text{TOD},k}, \quad (13)$$

is the i -th data point in the mock sample, N_i is its the number of TOD points and $T_{\text{TOD},k}$ is its k -th TOD point; and

$$T_{ik} = \frac{\sum_{l=1, l \neq k}^{N_i} T_{\text{TOD},l}}{N_i - 1}. \quad (14)$$

In Fig 5 we plot the above errors of our mock sample, compared with thermal noise. We find that such kind of error is larger than the thermal noise.

Another two errors of using Eq. (3) rise from the large area of constant sky temperature in the modeling with a limited number ($N_{\text{region}} = 12$) of sky regions in the reconstruction process, and the inaccuracy of the formula Eq. (6) in describing the spectra. The derived \bar{T}_j is different from the mean sky temperature in the region

$$\bar{T}_j(\nu) = \frac{1}{\Delta\Omega_j} \int_{\Delta\Omega_j} T_{\text{sky}}(\nu, \hat{\mathbf{k}}) d\Omega(\hat{\mathbf{k}}), \quad (15)$$

because the sky temperature varies within the region.

The error to fit the i -th mock data simple

$$\begin{aligned} \delta T_i &= \frac{1}{8\pi/3} \sum_{j=1}^{N_{\text{region}}} \left[\int_{\Delta\Omega_j} S(\hat{\mathbf{k}}, \hat{\mathbf{k}}_i) B(\hat{\mathbf{k}}, \hat{\mathbf{k}}_i) T_{\text{sky}}(\hat{\mathbf{k}}) d\Omega(\hat{\mathbf{k}}) \right. \\ &\quad \left. - \tilde{\mathcal{B}}_j \bar{T}_j \Delta\Omega_j \right] \\ &= \frac{1}{(8\pi/3)} \sum_{j=1}^{N_{\text{region}}} \left[\int_{\Delta\Omega_j} S(\hat{\mathbf{k}}, \hat{\mathbf{k}}_i) B(\hat{\mathbf{k}}, \hat{\mathbf{k}}_i) T_{\text{sky}}(\hat{\mathbf{k}}) d\Omega(\hat{\mathbf{k}}) \right. \\ &\quad \left. - \tilde{\mathcal{B}}_j \bar{T}_j \Delta\Omega_j + \tilde{\mathcal{B}}_j \bar{T}_j \Delta\Omega_j - \tilde{\mathcal{B}}_j \bar{T}_j \Delta\Omega_j \right] \\ &= \frac{1}{8\pi/3} \sum_{j=1}^{N_{\text{region}}} \left[\int_{\Delta\Omega_j} [S(\hat{\mathbf{k}}, \hat{\mathbf{k}}_i) B(\hat{\mathbf{k}}, \hat{\mathbf{k}}_i) - \tilde{\mathcal{B}}_j] T_{\text{sky}}(\hat{\mathbf{k}}) d\Omega(\hat{\mathbf{k}}) \right. \\ &\quad \left. + \sum_{j=1}^{N_{\text{region}}} (\bar{T}_j - \tilde{T}_j) \tilde{\mathcal{B}}_j \Delta\Omega_j \right] \\ &= \frac{1}{(8\pi/3)} \left[\int_{4\pi} [S(\hat{\mathbf{k}}, \hat{\mathbf{k}}_i) B(\hat{\mathbf{k}}, \hat{\mathbf{k}}_i) - \tilde{\mathcal{B}}(\hat{\mathbf{k}})] T_{\text{sky}}(\hat{\mathbf{k}}) d\Omega(\hat{\mathbf{k}}) \right. \\ &\quad \left. + \sum_{j=1}^{N_{\text{region}}} (\bar{T}_j - \tilde{T}_j) \tilde{\mathcal{B}}_j \Delta\Omega_j \right]. \end{aligned} \quad (16)$$

Further we define

$$\delta \tilde{\mathcal{B}}(\hat{\mathbf{k}}) = S(\hat{\mathbf{k}}, \hat{\mathbf{k}}_i) B(\hat{\mathbf{k}}, \hat{\mathbf{k}}_i) - \tilde{\mathcal{B}}(\hat{\mathbf{k}}), \quad (17)$$

	prior	$j = 1$	$j = 2$	$j = 3$	$j = 4$	$j = 5$	$j = 6$
(l, b)	–	$(45.0^\circ, 41.8^\circ)$	$(135.0^\circ, 41.8^\circ)$	$(225.0^\circ, 41.8^\circ)$	$(315.0^\circ, 41.8^\circ)$	$(0.0^\circ, 0.0^\circ)$	$(90.0^\circ, 0.0^\circ)$
$\log A_j$ [log K]	[8,20]	$16.20^{+0.49}_{-0.54}$	$16.41^{+0.39}_{-0.52}$	$16.06^{+0.49}_{-0.57}$	$15.54^{+0.64}_{-0.54}$	$14.52^{+0.23}_{-0.19}$	$14.59^{+0.31}_{-0.32}$
ν_j [MHz]	[0,7]	$2.44^{+0.62}_{-0.47}$	$2.16^{+0.44}_{-0.35}$	$1.89^{+0.52}_{-0.41}$	$2.98^{+0.83}_{-0.73}$	$6.16^{+0.61}_{-0.62}$	$5.21^{+0.64}_{-0.55}$
a_j	[-4,0]	$-2.39^{+0.10}_{-0.11}$	$-2.59^{+0.14}_{-0.19}$	$-2.30^{+0.11}_{-0.12}$	$-2.41^{+0.10}_{-0.11}$	$-2.26^{+0.06}_{-0.07}$	$-2.43^{+0.09}_{-0.10}$
b_j	[0,3]	$1.27^{+0.43}_{-0.38}$	$2.09^{+0.49}_{-0.53}$	$1.96^{+0.64}_{-0.63}$	$1.19^{+0.38}_{-0.34}$	$1.33^{+0.29}_{-0.22}$	$0.95^{+0.29}_{-0.26}$
	prior	$j = 7$	$j = 8$	$j = 9$	$j = 10$	$j = 11$	$j = 12$
(l, b)	–	$(180.0^\circ, 0.0^\circ)$	$(270.0^\circ, 0.0^\circ)$	$(45.0^\circ, -41.8^\circ)$	$(135.0^\circ, -41.8^\circ)$	$(225.0^\circ, -41.8^\circ)$	$(315.0^\circ, -41.8^\circ)$
$\log A_j$ [log K]	[8,20]	$14.10^{+0.30}_{-0.25}$	$13.91^{+0.32}_{-0.29}$	$16.20^{+0.42}_{-0.48}$	$16.63^{+0.30}_{-0.37}$	$16.36^{+0.41}_{-0.53}$	$14.92^{+0.90}_{-0.71}$
ν_j [MHz]	[0,7]	$5.91^{+0.70}_{-0.78}$	$6.07^{+0.61}_{-0.69}$	$2.29^{+0.57}_{-0.44}$	$1.80^{+0.30}_{-0.24}$	$1.95^{+0.43}_{-0.27}$	$3.42^{+1.00}_{-0.96}$
a_j	[-4,0]	$-2.47^{+0.12}_{-0.13}$	$-2.51^{+0.15}_{-0.16}$	$-2.42^{+0.10}_{-0.10}$	$-2.35^{+0.09}_{-0.10}$	$-2.56^{+0.17}_{-0.18}$	$-2.28^{+0.15}_{-0.15}$
b_j	[0,3]	$1.34^{+0.33}_{-0.26}$	$1.59^{+0.36}_{-0.32}$	$1.51^{+0.53}_{-0.45}$	$2.35^{+0.44}_{-0.60}$	$2.30^{+0.47}_{-0.64}$	$1.36^{+0.47}_{-0.45}$

Table 1. The best-fit values (defined as the medians of the marginal distributions) and 1σ uncertainties of the spectrum parameters for the 12 regions.

Then the first term of Eq. (16) is

$$\sum_{l=0}^{l_{\max}} \sum_{m=-l}^l \delta\tilde{\mathcal{B}}_{lm}^* T_{\text{sky},lm}, \quad (18)$$

where $\delta\tilde{\mathcal{B}}_{lm}$ and $T_{\text{sky},lm}$ are Spherical Harmonic transforms of $\delta\tilde{\mathcal{B}}(\hat{\mathbf{k}})$ and $T_{\text{sky}}(\hat{\mathbf{k}})$ respectively. The contribution of the first term in Eq. (16) to the covariance matrix is

$$\begin{aligned} C_{i_1 i_2}^p &= \left(\sum_{l,m} \delta\tilde{\mathcal{B}}_{lm}^*(i_1) T_{\text{sky},lm} \right) \left(\sum_{l',m'} \delta\tilde{\mathcal{B}}_{l'm'}^*(i_2) T_{\text{sky},l'm'} \right)^* \\ &= \sum_{l,m} \sum_{l',m'} \delta\tilde{\mathcal{B}}_{lm}^*(i_1) \delta\tilde{\mathcal{B}}_{l'm'}(i_2) T_{\text{sky},lm} T_{\text{sky},l'm'}^*. \end{aligned} \quad (19)$$

We assume the sky has the properties so that the following approximation holds (m modes are independent of l modes),

$$\begin{aligned} C_{i_1 i_2}^p &\approx \sum_{lm} \sum_{l'm'} \delta\tilde{\mathcal{B}}_{lm}^*(i_1) \delta\tilde{\mathcal{B}}_{l'm'}(i_2) T_{\text{sky},lm} T_{\text{sky},l'm'}^* \delta_{ll'} \delta_{mm'} \\ &= \sum_{lm} \delta\tilde{\mathcal{B}}_{lm}^*(i_1) \delta\tilde{\mathcal{B}}_{lm}(i_2) T_{\text{sky},lm} T_{\text{sky},lm}^*, \end{aligned} \quad (20)$$

where $\delta_{ll'}$ and $\delta_{mm'}$ are Kronecker deltas. For isotropic distribution of sky temperature fluctuations in each region, above formula has further approximation

$$\begin{aligned} C_{i_1 i_2}^p &\approx \sum_{lm} \delta\tilde{\mathcal{B}}_{lm}^*(i_1) \delta\tilde{\mathcal{B}}_{lm}(i_2) \langle T_{\text{sky},lm} T_{\text{sky},lm}^* \rangle_m, \\ &= \sum_{lm} \delta\tilde{\mathcal{B}}_{lm}^*(i_1) \delta\tilde{\mathcal{B}}_{lm}(i_2) C_l \end{aligned} \quad (21)$$

where

$$\begin{aligned} C_l &= \frac{1}{2l+1} \sum_m T_{\text{sky},lm} T_{\text{sky},lm}^* \\ &= \langle T_{\text{sky},lm} T_{\text{sky},lm}^* \rangle_m \end{aligned} \quad (22)$$

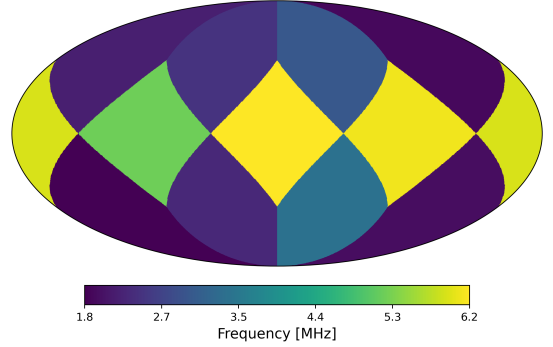


Figure 7. The turnover frequency ν_j for the 12 regions on sky.

is the angular power spectrum of the sky temperature. Note that the covariance matrix is not necessarily diagonal. In Fig. 6 we plot $C_{i_1 i_2}^p$ in units of K².

The second term of Eq. (16) is the error when using Eq. (6) to fit the mean frequency spectrum of each region. We use a constant 10% to represent this error, according to the directly fitting errors tested with ULSA, say

$$C_{ij}^m = \begin{cases} (0.1\bar{T}_{\text{sky},i})^2, & i = j \\ 0, & i \neq j. \end{cases} \quad (23)$$

Finally, the full covariance matrix is the sum of C^n (Eq. (9)), C^a (Eq. (12)), C^p (Eq. (21)), and C^m (Eq. (23)).

3. RESULTS

In Tab. 1 we list the fitting results of the frequency spectrum parameters for the 12 regions. Among these parameters, ν_j reflects the typical frequency where spectrum turnover happens. We find that regions closer to the Galactic plane have a larger ν_j , which means that the absorption is stronger at low Galactic latitude re-

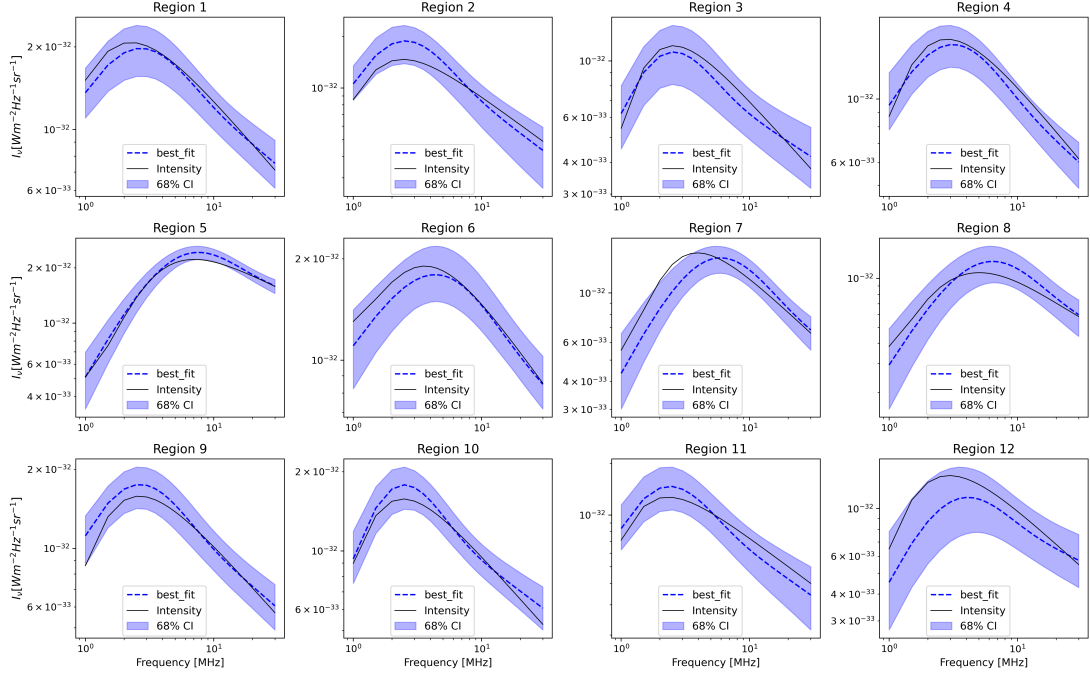


Figure 8. The fitted spectra for the 12 regions. To highlight the turnover feature on the spectrum, we convert the brightness temperature into the specific intensity via Rayleigh–Jeans law. In each panel, solid line is the mean intensity of the region from ULSA sky model; dashed line is the median spectrum and shaded region refers to the 1σ uncertainty.

gions. For the region near the Galactic Center, ν_j can be up to ~ 6 MHz; while for the high Galactic latitude region at the southwest sky (i.e. $j = 10$), ν_j is as low as ~ 2 MHz. The uncertainty on the derived ν_j is typically $\sim 10\% - 30\%$. The single-antenna observations, via the lunar occultation and thanks to the anisotropy of antenna primary beam response, are indeed feasible to recover the free-free absorption for different parts of the Milky Way.

In Fig. 7 we plot ν_j of the 12 regions on the sky map. It shows more clearly that near the Galactic plane ν_j is larger than at high Galactic latitudes. This is expected, because the density of the ISM is higher at the Galactic plane, and there are more HII regions generated from massive stars and supernova remnants (e.g. Cordes & Lazio 2002, 2003; Reynolds 2004; Gaensler et al. 2008; Yao et al. 2017; Ocker et al. 2021).

In Fig. 8 we plot the fitted spectra and uncertainties for the 12 regions, compared with spectra from ULSA sky model. We convert the sky brightness temperature into the specific intensity using Rayleigh-Jeans law, to show the absorption-induced turnover feature more intuitively. In all regions, the fitted spectrum agrees with the input sky model, and the turnover feature appears clearly. Moreover, we find that the uncertainties vary significantly among different regions and different frequencies, from $\sim 10\%$ up to $\sim 40\%$, with the largest uncertainty appears at the lowest frequencies.

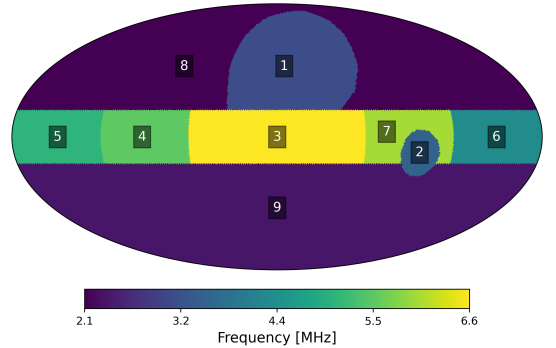


Figure 9. The turnover frequency ν_j for the 9 regions with labeled sequence on each pixel.

To further investigate the origins of uncertainties, we manually divide the sky into 9 representative regions: Loop I, the northern high-Galactic-latitude region, the southern high-Galactic-latitude region, the Galactic center, the Gum nebula, and four other Galactic plane regions ($l \sim \pm 90^\circ$ and $l \sim \pm 135^\circ$, respectively), as illustrated in Fig. 9.

The best-fit values for the parameters are listed in Tab. 2, and the fitted spectra and uncertainties are shown in Fig. 10. We find that for both Loop I and northern and southern high-Galactic-latitude regions, the best-fit spectra agree very well with the mean sky temperature, and the uncertainties are small. However, for regions close to the Galactic plane, at frequencies be-

	prior	$j = 1$	$j = 2$	$j = 3$	$j = 4$	$j = 5$
$\log A_j$ [log K]	[8,20]	$15.70^{+0.67}_{-0.66}$	$11.62^{+2.51}_{-2.42}$	$14.48^{+0.13}_{-0.09}$	$14.72^{+0.58}_{-0.35}$	$14.65^{+0.68}_{-0.44}$
ν_j [MHz]	[0,7]	$3.14^{+1.08}_{-0.83}$	$3.49^{+1.44}_{-2.00}$	$6.62^{+0.28}_{-0.48}$	$5.50^{+1.05}_{-1.42}$	$5.04^{+1.22}_{-1.50}$
a_j	[-4,0]	$-2.50^{+0.11}_{-0.11}$	$-1.98^{+1.08}_{-1.04}$	$-2.25^{+0.07}_{-0.06}$	$-2.49^{+0.19}_{-0.24}$	$-2.44^{+0.19}_{-0.21}$
b_j	[0,3]	$1.21^{+0.51}_{-0.38}$	$1.23^{+1.14}_{-0.89}$	$1.53^{+0.37}_{-0.30}$	$1.40^{+0.68}_{-0.52}$	$1.62^{+0.69}_{-0.65}$
	prior	$j = 6$	$j = 7$	$j = 8$	$j = 9$	
$\log A_j$ [log K]	[8,20]	$14.75^{+0.78}_{-0.65}$	$13.95^{+0.49}_{-0.52}$	$16.18^{+0.29}_{-0.45}$	$15.97^{+0.27}_{-0.35}$	
ν_j [MHz]	[0,7]	$4.28^{+1.50}_{-1.38}$	$6.00^{+0.72}_{-1.35}$	$2.10^{+0.48}_{-0.28}$	$2.36^{+0.43}_{-0.29}$	
a_j	[-4,0]	$-2.44^{+0.21}_{-0.27}$	$-2.34^{+0.33}_{-0.36}$	$-2.41^{+0.05}_{-0.06}$	$-2.42^{+0.04}_{-0.05}$	
b_j	[0,3]	$1.49^{+0.68}_{-0.62}$	$1.35^{+1.02}_{-0.84}$	$1.73^{+0.51}_{-0.45}$	$1.58^{+0.35}_{-0.28}$	

Table 2. Similar to Tab. 1, however the sky is divided into 9 regions with different areas as illustrated in Fig. 9.

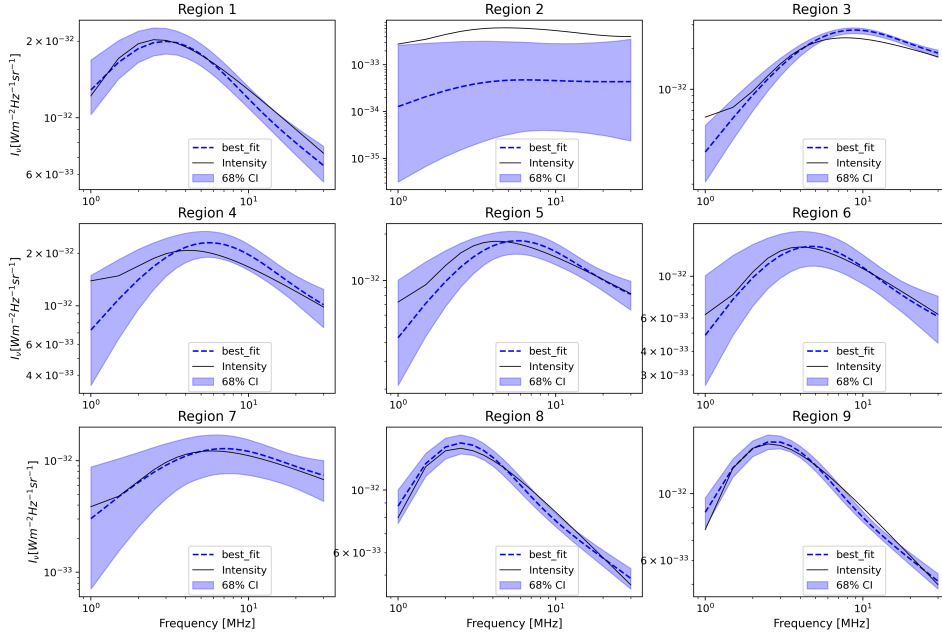


Figure 10. The fitted spectra for the 9 regions as illustrated in Fig. 9. The line labels are the same as in Fig. 8.

low ~ 2 MHz, Eq. (6) fails to describe the mean sky temperature because the absorption is strong (Cong et al. 2021), and this is the main source of uncertainties. For the Gum nebula, the uncertainty is obviously larger than other regions, because this exceptionally dense structure breaks our assumption about the uncertainty of Eq. (21). Moreover, it is interesting to note that Loop I is not very different from the vicinity high Galactic latitude regions.

4. SUMMARY AND DISCUSSION

In this paper, we reconstructed the frequency spectra for different sky regions from mock observational data for a single antenna lunar-orbit satellite. The satellite is assumed to be one of the DSL low-frequency satellites. Thanks to the lunar occultation of the sky and the anisotropy of the antenna primary beam response, the sky temperature received by antenna varies with its

pointing, providing us with the information of sky temperature anisotropy. Moreover, orbital precession avoids the antenna repeatedly point to same direction in one precession period (1.3 yr for DSL) that is much longer than the orbital period (2.3 hr for DSL). This breaks the symmetry above and below the satellite orbital plane, further providing information about the sky temperature anisotropy.

We generated mock observational data simple from ULSA sky model in one precession period, and modeled various uncertainties. We then found the best-fit parameterized frequency spectra of different sky regions simultaneously, using the MCMC method. Compared with the sky model, we correctly reconstructed all spectra and derived the absorption feature (the turnover frequency) toward different directions on sky. Near the Galactic plane, the turnover frequency is larger, which

means that the absorption is stronger. At high Galactic latitude regions, the turnover frequency is smaller and the absorption is weaker. Our investigation proves that single antenna lunar-orbit experiment has the ability to reconstruct the anisotropic frequency spectrum. It will largely extend the application of the upcoming single antenna data of DSL low frequency satellites, or any single antenna lunar-orbit satellites that work in ultra-long wavelength band.

In Cong et al. (2022) it was proposed that the 3D electron distribution in Milky Way can be reconstructed from ultra-long wavelength spectra for different directions. However, that algorithm requires high angular

resolution of multi-frequency sky map, up to $\sim 1^\circ$ level. The spectra reconstructed from single antenna observations cannot be directly applied in this methods. However, if the electron distribution is well parameterized (e.g. Cordes et al. 1991), the constraints on the model parameters can be derived.

ACKNOWLEDGMENTS

This work was supported by National Key R&D Program of China No. 2022YFF0504300, and NSFC International (Regional) Cooperation and Exchange Project No. 12361141814.

REFERENCES

- Alexander, J. K., Brown, L. W., Clark, T. A., Stone, R. G., & Weber, R. R. 1969, *ApJL*, 157, L163, doi: [10.1086/180411](https://doi.org/10.1086/180411)
- Alexander, J. K., & Stone, R. G. 1965, *ApJ*, 142, 1327, doi: [10.1086/148418](https://doi.org/10.1086/148418)
- Bale, S. D., Bassett, N., Burns, J. O., et al. 2023, arXiv e-prints, arXiv:2301.10345, doi: [10.48550/arXiv.2301.10345](https://doi.org/10.48550/arXiv.2301.10345)
- Bassett, N., Rapetti, D., Nhan, B. D., et al. 2023, *ApJ*, 945, 134, doi: [10.3847/1538-4357/acbc76](https://doi.org/10.3847/1538-4357/acbc76)
- Brown, L. W. 1973, *ApJ*, 180, 359, doi: [10.1086/151968](https://doi.org/10.1086/151968)
- Burns, J., Hallinan, G., Chang, T.-C., et al. 2021a, arXiv e-prints, arXiv:2103.08623, doi: [10.48550/arXiv.2103.08623](https://doi.org/10.48550/arXiv.2103.08623)
- Burns, J., Bale, S., Bradley, R., et al. 2021b, arXiv e-prints, arXiv:2103.05085, doi: [10.48550/arXiv.2103.05085](https://doi.org/10.48550/arXiv.2103.05085)
- Cane, H. V. 1979, *Monthly Notices of the Royal Astronomical Society*, 189, 465, doi: [10.1093/mnras/189.3.465](https://doi.org/10.1093/mnras/189.3.465)
- Chen, X., Yan, J., Deng, L., et al. 2021, *Philosophical Transactions of the Royal Society A: Mathematical, Physical and Engineering Sciences*, 379, 20190566, doi: [10.1098/rsta.2019.0566](https://doi.org/10.1098/rsta.2019.0566)
- Chen, X., Burns, J., Koopmans, L., et al. 2019, arXiv e-prints, arXiv:1907.10853, doi: [10.48550/arXiv.1907.10853](https://doi.org/10.48550/arXiv.1907.10853)
- Cong, Y., Yue, B., Xu, Y., et al. 2021, *The Astrophysical Journal*, 914, 128, doi: [10.3847/1538-4357/abf55c](https://doi.org/10.3847/1538-4357/abf55c)
- Cong, Y., Yue, B., Xu, Y., Shi, Y., & Chen, X. 2022, *ApJ*, 940, 180, doi: [10.3847/1538-4357/ac9df7](https://doi.org/10.3847/1538-4357/ac9df7)
- Cordes, J., Weisberg, J., Frail, D., Spangler, S., & Ryan, M. 1991, *Nature*, 354, 121
- Cordes, J. M., & Lazio, T. J. W. 2002, arXiv e-prints, astro, doi: [10.48550/arXiv.astro-ph/0207156](https://doi.org/10.48550/arXiv.astro-ph/0207156)
- . 2003, arXiv e-prints, astro, doi: [10.48550/arXiv.astro-ph/0301598](https://doi.org/10.48550/arXiv.astro-ph/0301598)
- Ellis, G. R. A., & Hamilton, P. A. 1966, *ApJ*, 143, 227, doi: [10.1086/148493](https://doi.org/10.1086/148493)
- Foreman-Mackey, D., Hogg, D. W., Lang, D., & Goodman, J. 2013, *Publications of the Astronomical Society of the Pacific*, 125, 306, doi: [10.1086/670067](https://doi.org/10.1086/670067)
- Gaensler, B., Madsen, G., Chatterjee, S., & Mao, S. 2008, *Publications of the Astronomical Society of Australia*, 25, 184
- Gorski, K. M., Hivon, E., Banday, A. J., et al. 2005, *The Astrophysical Journal*, 622, 759, doi: [10.1086/427976](https://doi.org/10.1086/427976)
- Jester, S., & Falcke, H. 2009, *NewAR*, 53, 1, doi: [10.1016/j.newar.2009.02.001](https://doi.org/10.1016/j.newar.2009.02.001)
- Novaco, J. C., & Brown, L. W. 1978, *ApJ*, 221, 114, doi: [10.1086/156009](https://doi.org/10.1086/156009)
- Ocker, S. K., Cordes, J. M., & Chatterjee, S. 2021, *The Astrophysical Journal*, 911, 102
- Page, B., Bassett, N., Lecacheux, A., et al. 2022, *A&A*, 668, A127, doi: [10.1051/0004-6361/202244621](https://doi.org/10.1051/0004-6361/202244621)
- Peterson, J. D., & Webber, W. R. 2002, *The Astrophysical Journal*, 575, 217, doi: [10.1086/341258](https://doi.org/10.1086/341258)
- Quenouille, M. H. 1949, *Journal of the Royal Statistical Society: Series B (Methodological)*, 11, 68, doi: [10.1111/j.2517-6161.1949.tb00023.x](https://doi.org/10.1111/j.2517-6161.1949.tb00023.x)
- Reynolds, R. 2004, *Advances in Space Research*, 34, 27
- Shi, Y., Deng, F., Xu, Y., et al. 2022a, *The Astrophysical Journal*, 929, 32, doi: [10.3847/1538-4357/ac5965](https://doi.org/10.3847/1538-4357/ac5965)
- Shi, Y., Xu, Y., Deng, L., et al. 2022b, *Monthly Notices of the Royal Astronomical Society*, 510, 3046, doi: [10.1093/mnras/stab3623](https://doi.org/10.1093/mnras/stab3623)
- Smith, F. G. 1965, *MNRAS*, 131, 145, doi: [10.1093/mnras/131.1.145](https://doi.org/10.1093/mnras/131.1.145)
- Tukey, J. W. 1958, *Ann.math.statist*, 29, 614

Yao, J. M., Manchester, R. N., & Wang, N. 2017, *ApJ*, 835,
29, doi: [10.3847/1538-4357/835/1/29](https://doi.org/10.3847/1538-4357/835/1/29)

Yates, K. W., & Wielebinski, R. 1967, *ApJ*, 149, 439,
doi: [10.1086/149269](https://doi.org/10.1086/149269)